Numerical simulation on residual thickness of pipes with curved sections in water-assisted co-injection molding

Tang-Qing Kuang,[1] Bai-Ping Xu,[2] Guo-Fa Zhou,[3] Lih-Sheng Turng[4]

[1]School of Mechanical & Electrical Engineering, East China Jiaotong University, Nanchang 330013, China
[2]Technology Development Center for Polymer Processing Engineering of Guangdong Colleges and Universities, Guangdong Industry Technical College, Guangzhou 510641, China
[3]School of Environmental and Chemical Engineering, Nanchang University, Nanchang 330000, China
[4]Polymer Engineering Center and Wisconsin Institute for Discovery, University of Wisconsin–Madison, Madison 53706, Wisconsin
Correspondence to: L.-S. Turng (E-mail: turng@engr.wisc.edu)

ABSTRACT: The residual thicknesses of the skin and the inner layers are important quality indicators of water-assisted co-injection molding (WACIM) process or overflow WACIM (O-WACIM) parts. At the curved section, the residual thicknesses change significantly. A numerical simulation program based on the computational fluid dynamics method was developed to simulate the O-WACIM process. After the numerical simulation program was validated with the experimental results, it was used to study the effects of the bending radii and bending angles on the residual thicknesses of the skin and inner layers of O-WACIM parts. The results showed that the penetration of the inner melt and water was always close to the inner concave side due to the higher local pressure gradient and temperature. The effects of processing parameters on the residual thicknesses of the skin and inner layers were investigated using the orthogonal simulation method. It was found that the residual thicknesses of the skin/inner layer at the inner concave/outer convex side are mainly influenced by different parameters. © 2015 Wiley Periodicals, Inc. J. Appl. Polym. Sci. **2015**, *132*, 42468.

INTRODUCTION

Water-assisted co-injection molding (WACIM), an innovative plastic injection molding technology used to produce hollow plastic parts with a multilayer structure, was first developed in Germany several years ago.[1] WACIM can be considered a combined processing technology of water-assisted injection molding (WAIM) and co-injection molding (CIM) processes. WACIM can be categorized into two types: short-shot WACIM (S-WACIM) and overflow WACIM (O-WACIM). In the S-WACIM process, the mold cavity is partially filled with two different polymer melts, which are injected sequentially and form a skin/core structure, followed by the injection of water into the core of the polymer melt. Figure 1(a) shows the schematic diagram of the S-WACIM process. S-WACIM parts have some defects such as a switchover mark on the product surface and potentially uneven residual wall thicknesses in the flow direction.[2] In the O-WACIM process, the mold cavity is first completely filled with polymer melt, followed by a high-pressure fluid that pushes the material into an overflow cavity. Figure 1(b) shows the O-WACIM process schematically.

WACIM has the advantages of both WAIM and CIM, such as greater freedom of design, material savings, weight reduction, cost savings, and comprehensive performance of different materials.[3–7] Moreover, it offers a wide-processing window.[1] Currently, WACIM technology is mainly used for automotive, household, and furniture items, highlighting a bright future for WACIM with regard to market prospects.

Many researchers have investigated the penetration behaviors of water, the distribution of the residual wall thickness,[8–12] and the optimization of processing parameters in WAIM via experimentation.[13–15] Some scholars have studied the primary and secondary penetration of WAIM via numerical simulations.[16,17] Polynkin et al.[9] and Khor et al.[18] have used FLUENT to handle the injection mold filling problems. Zhang et al.[19] simulated the mold filling behavior during the WAIM process with the Giesekus viscoelastic model. Few researchers have investigated the influence of processing parameters on the WACIM process using the numerical simulation method.[20–22] Kuang et al.[23] studied the WACIM of noncircular pipes by numerical simulation and experimentation. Most of the studies mentioned above
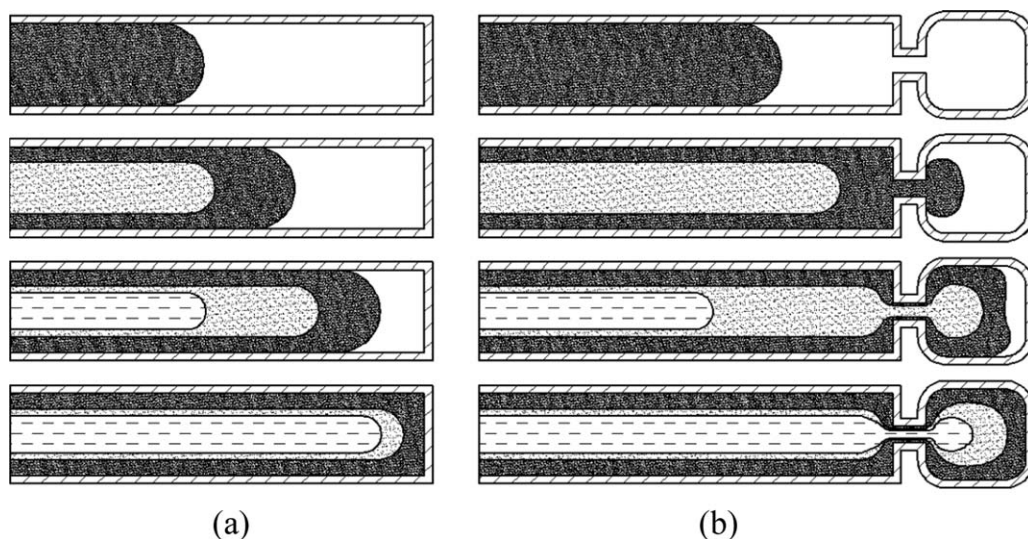
Figure 1. Schematic diagram of WACIM processes: (a) S-WACIM and (b) O-WACIM.

were focused on the results at the constant cross-sections. Liu et al.[24] investigated the WACIM of plastic pipes with dimensional transitions by experimentation. Lin et al.[25] used differential mold temperatures to improve the residual wall thickness uniformity around curved sections of fluid-assisted injection-molded pipes. Park et al.[5] studied the void formation in the residual wall thickness of fluid-assisted injection molding parts with curved sections. Yang et al.[26] investigated the residual wall thickness of pipes with dimensional transitions and curved sections in WAIM via numerical simulation.

The main products of WACIM are pipes and beams. While the extrusion process can only produce straight pipes, WACIM can fabricate pipes with dimensional transitions, curved sections, and multiple layers. Obviously, residual wall thickness significantly affects the quality of molded pipes. To the best knowledge of the authors, the residual wall thickness at the curved sections of the WACIM pipes has not been systematically studied.

This present research is devoted to studying the effects of geometry, including bending radius and angle, and the processing parameters on the residual thicknesses of the skin and inner layers around the curved sections of the O-WACIM pipes. The CFD method was used to simulate the O-WACIM process and the free interfaces of the skin–inner melt, with the inner melt–water interfaces being tracked by the volume of fluid (VOF) method. This study mainly included the following: (1) Validating the simulation of the penetration behaviors of the inner melt and water at the curved sections and identifying the mechanism. (2) Studying the geometrical effects of bending radius and bending angle on the residual wall thickness around curved sections. (3) Studying the effect of processing parameters on the residual wall thickness around curved sections. The simulation results in terms of the skin layer for a curved pipe sample part were in good agreement with the experimental data. After the simulation result was validated and deemed reliable, a numerical design of experiments (DOE) study was conducted over a wide range of geometry and processing parameters to generate

helpful insights into the design and molding of WACIM pipes with curved sections. It was found that the penetration of the inner melt and water was always close to the inner concave side due to the higher local pressure gradient and temperature. It was also found that the residual thicknesses of the skin/inner layer at the inner concave/outer convex side were mainly influenced by some of the mold temperature, the inner melt injection delay time, the inner melt temperature, the water injection delay time, and the water injection velocity.

MODEL AND METHOD

Mathematical Model

To simplify the flow process and facilitate the CFD simulation, the following simplifications and assumptions for WACIM were made:

1. Initially, the skin melt (the first injected melt) fills the mold cavity uniformly; it does not affect the following penetrations of the inner melt and water.
2. The melt and the water are considered incompressible, which is reasonable for the filling stage. Properties such as density, heat capacity, and thermal conductivity are assumed to be constants.[27,28]
3. The melt flow has a no-slip boundary. The body force is taken into consideration, while the surface tension is ignored.

Governing equations for the filling stage of WACIM include the continuity equation, momentum equation, energy equation, constitutive equation, viscosity model, and volume fraction equation.

The continuity equation deals with the law of mass conservation and is expressed as

$$\frac{\partial \rho}{\partial t} + \frac{\partial}{\partial x_i}(\rho u_i) = 0 \tag{1}$$

The random nature of the turbulent flow must be considered in the momentum equation for the high Reynold's number (high

turbulence) of water. Therefore, an additional Reynold's stresses term was introduced in the momentum equation typically used for traditional injection molding. The Reynold's time-averaged momentum equation becomes,

$$\frac{\partial}{\partial t}(\rho u_i) + \frac{\partial}{\partial x_j}(\rho u_i u_j) = \frac{\partial}{\partial x_j}\left[\mu\left(\frac{\partial u_i}{\partial x_j} + \frac{\partial u_j}{\partial x_i} - \frac{2}{3}\delta_{ij}\frac{\partial u_l}{\partial x_l}\right)\right]$$
$$- \frac{\partial p}{\partial x_i} + \rho f + \frac{\partial}{\partial x_j}\left(-\rho\overline{u_i'u_j'}\right) \quad (2)$$

where f denotes the body force, and the last item corresponds to the Reynold's stress.

Based on the Boussinesq eddy viscosity assumption,[29] the relationship between the Reynold's stress and the average velocity gradient is

$$-\rho\overline{u_i'u_j'} = \mu_t\left(\frac{\partial u_i}{\partial x_j} + \frac{\partial u_j}{\partial x_i}\right) - \frac{2}{3}\left(\rho k + \mu\frac{\partial u_i}{\partial x_j}\right)\delta_{ij} \quad (3)$$

where μ_t denotes the turbulent viscosity, and k denotes the turbulent kinetic energy.

Water penetration is simulated using the standard $k-\omega$ two-equation turbulence model, which has proven to be more suitable than the $k-\varepsilon$ model used to describe the flow field of WAIM.[17]

The heat exchange between the water and the melt is considered in the injection process. The energy equation is expressed as

$$\frac{\partial(\rho E)}{\partial t} + \frac{\partial}{\partial x_j}[u_i(\rho E + p)] = \frac{\partial}{\partial x_j}\left[\lambda_{eff}\frac{\partial T}{\partial x_j} + u_i(\tau_{ij})_{eff}\right] \quad (4)$$

where E denotes the fluid total energy, p denotes the melt pressure, λ_{eff} denotes the effective thermal conductivity coefficient, and $(\tau_{ij})_{eff}$ denotes the deviatory stress tensor.

In WACIM, the melt flow in the mold cavity is predominantly shear flow and is mainly affected by the shear stress. Therefore, the elastic behavior of the melt is ignored and the generalized Newtonian fluid constitutive model is used for the WACIM simulation. In this study, the generalized Newtonian constitutive equation is used:

$$\tau = \eta(\dot{\gamma}, T, p)\dot{\gamma} \quad (5)$$

where T is the temperature and $\dot{\gamma}$ is the shear rate tensor.

The cross–WLF viscosity model,[30] which is a seven-constant model and can characterize a wide range of fluid viscosities, is used in the simulations of WACIM process:

$$\eta(\dot{\gamma}, T, p) = \frac{\eta_0(T, p)}{1 + (\eta\dot{\gamma}/\tau^*)^{1-n}} \quad (6)$$

$$\eta_0(T, p) = D_1 exp\left(-\frac{A_1(T-T^*)}{A_2 + (T-T^*)}\right) \quad (7)$$

$$T^*(p) = D_2 + D_3 p \quad (8)$$

$$A_2 = \bar{A}_2 + D_3 p \quad (9)$$

where η_0 denotes the zero shear viscosity; τ^* is the critical shear stress at the transition between Newtonian and power-law behavior; n denotes the power-law index; D_1, D_2, D_3, A_1, and $\bar{A}_2$ are all the material constants.

Table I. Cross–WLF Model Constants for the Materials Used in the Simulations

	HDPE	PP
τ^*(Pa)	5.73e + 004	24075
n(Pa)	0.2837	0.2921
D_1(Pa•s)	1.71e + 018	2.02e + 015
D_2(K)	153.2	263.15
D_3(K/Pa)	0	0
A_1	35.357	33.242
$\bar{A}_2$(K)	51.6	51.6

For the illustrative simulation cases, the molding material for the skin is high-density polyethylene (HDPE, Rigidex HM5420XP, BP Chemicals Corp.), while the inner material was polypropylene (PP, Globalene PC366, Taiwan PP Corp.). Their cross–WLF viscosity model parameters, which were obtained from the Moldflow material library, are listed in Table I.

Because the outer skin and inner core melts and the water are free surface flows without mutual penetration between these three phases, the free interfaces of the skin melt–inner melt and the inner melt–water were tracked by the VOF method. The continuity equation of the volume fraction is given by

$$\frac{\partial F_i}{\partial t} + \boldsymbol{u} \cdot \nabla F_i = 0 \quad (10)$$

where F_i is the volume fraction of the ith phase, which varies between 0 and 1. The sum of all of the phases' volume fractions is equal to 1. F_i takes the value of 1 for cells that contain only the i phase and the value of 0 when it is the void of the i phase. A cell partially filled with the phase will have a value between 0 and 1, which represents the i phase front. In this study, the value 0.5 of F_i is treated as the interface of the i phase front.

Molded Parts and Processing Parameters
Recall that for the O-WACIM process studied here, the mold cavity was completely filled with the skin melt. After a short switch over time, the inner melt was injected to penetrate into the core of the skin melt. When the inner melt reached the overflow outlet, the injection of the inner melt is terminated. After a preset delay time, water was injected to penetrate into the core of the inner melt until it reached the overflow outlet. All of the displaced melt went through the outlet into the overflow cavity.

A pipe with three curved sections was chosen as the test case. The residual thicknesses of the skin layer and the inner layer were calculated at eleven positions, i.e., P1 to P11, as shown in Figure 2. The bending radius R was 18 mm. The corresponding residual thicknesses of the experimental samples were measured using a digital Vernier caliper with a minimum resolution of 0.01 mm. The measured residual thickness was a mean value, which was obtained by averaging the values of five samples. The processing parameters used in the simulation and experiment of the test case are listed in Table II.

In order to numerically investigate the effects of the bending angle and radius on the residual thicknesses of the skin layer
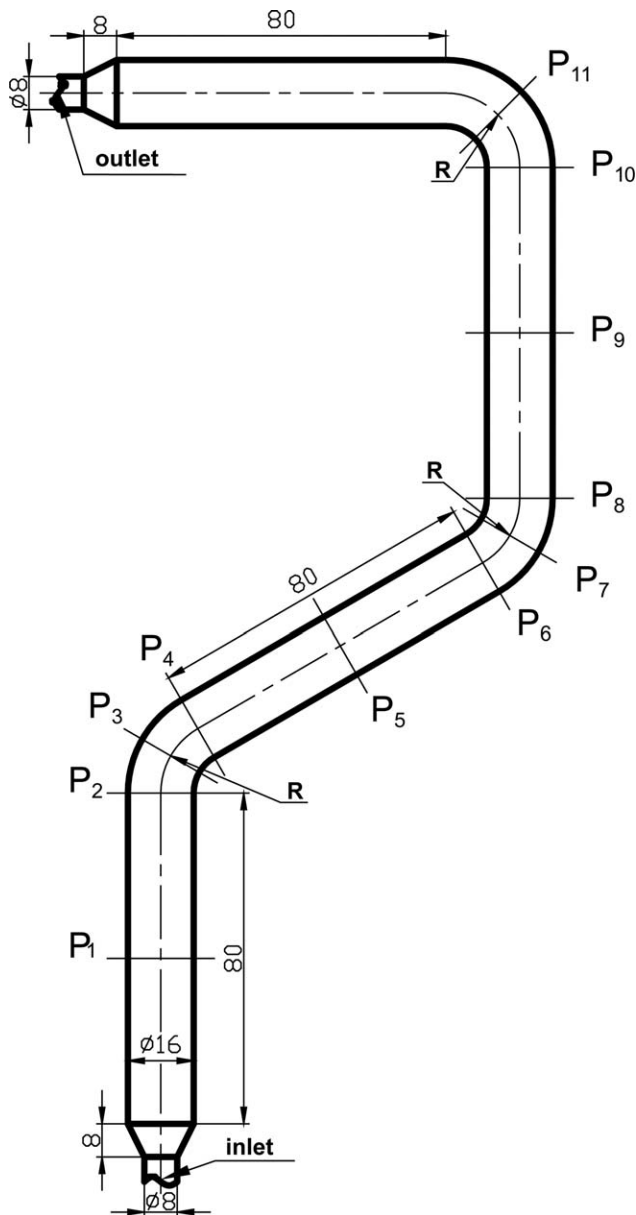
Figure 2. Schematic of molded curved pipe sample and positions for measuring the residual thicknesses. All dimensions are in millimeters.

Figure 3. Schematic of a pipe with one curved section and positions for measuring the residual thicknesses. All dimensions are in millimeters.

effects of the bending radius and the bending angle on the residual thickness around the curved section was investigated using simulation. The value of the geometry parameters are shown in Table III. The values of the processing parameters used in the investigation of the effect of geometry on the residual wall thickness are tabulated in Table IV.

A pipe with a 90° bending angle and an 18 mm bending radius was chosen and an orthogonal array of simulation runs based on the Taguchi method were conducted to study the effects of processing parameters on the residual wall thickness around the curved section. Seven processing parameters including mold temperature, inner melt temperature, inner melt (switch over) delay time, inner melt injection velocity, water temperature, water delay time, and water injection velocity were selected. Three levels for each factor were chosen using the Taguchi method as shown in Table V. The eighteen cases/runs, which were based on the orthogonal array $L_{18}(3^7)$, were conducted.

Boundary Conditions and Initial Conditions
Both boundary and initial conditions must be given to solve the mathematical model. Boundary conditions mainly include the velocity, temperature, and/or pressure at the inlet, outlet, and wall boundaries, which are shown in Figures 2 and 3 and specified as follows.

At the inlet: The velocity inlet boundary condition is specified, the temperature is assumed to be uniform, and the volume fraction of the cells at the inlet occupied by the fluid beginning to be injected is defined as 1, i.e.,

$$u=u_{inner}, T=T_{inner}, F_{inner}=1 \qquad t \in t_{inner} \qquad (11)$$

$$u=u_{water}, T=T_{water}, F_{water}=1 \qquad t \in t_{water} \qquad (12)$$

where t_{inner} and t_{water} are the stages of the inner melt and water injection, respectively.

At the outlet: The pressure is specified as the atmospheric pressure.

and the inner layer at the curved section, a shorter section of the pipe with just one curved section was modeled, as shown in Figure 3. The variables θ and R were the bending angle and bending radius, respectively. The residual thicknesses of the skin layer and the inner layer were calculated at the position P1, which was located in the middle of the curved section, as shown in Figure 3. Both the bending radius and the bending angle were variable. Keeping one constant and the other variable, the
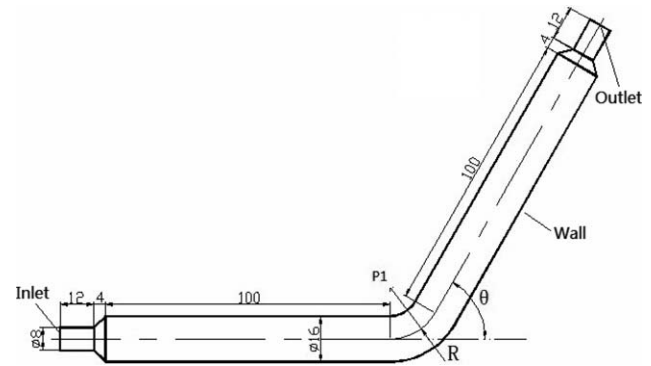
Table II. Processing Parameters Used in the Simulations of the Test Tube

Mold temp. (K)	Skin melt temp. (K)	Inner melt delay time(s)	Inner melt temp. (K)	Inner melt injection velocity (m/s)	Water delay time (s)	Water temp. (K)	Water injection velocity (m/s)
360	500	1	500	1.5	15	300	0.5

Table III. Geometry Parameters Used in the Simulations of Variable Geometries

θ (bending angle)	R (bending radius)
0°, 30°, 60°, 90°, 120°, 150°, 180°	18 mm
90°	1.5r, 2.0r, 2.5r, 3.0r, 3.5r, 4.0r, 4.5r

r is the radius of the pipe.

At the wall: The no-slip boundary condition is specified, and the temperature at the wall is fixed.[27,28]

Initial conditions mainly initialize the flow field. At the moment when the inner melt is injected into the cavity, the volume fraction of both the inner melt and water is 0, and the volume fraction of the skin melt is 1.

Numerical Procedure

Due to the round cross-section and axis-symmetry of the pipes, a two-dimensional simulation model was built. ANSYS Design Modeler and ANSYS Meshing were used to build the geometric model and discretize it into the mesh, respectively. The model was discretized with quadrilateral meshes with a mesh edge size of 0.4 mm. The numerical simulations were computed with ANSYS FLUENT14.5, where the governing equations were solved using the finite volume method. Some user-defined functions (UDFs) were programmed to impose the boundary conditions and time steps at different stages, calculate the viscosities of the melts, and record the filling times of the melt and water.

The multi-fluid VOF model was chosen and the free interfaces were tracked using the VOF method. The solver was a first-order implicit unsteady formulation. To improve accuracy, the PISO algorithm, which is suitable for unsteady flow, was adopted to solve the pressure–velocity coupling equation. For convergence and smoothness of solutions, the time step size during the filling stage was fixed as 0.0005 s, but was much longer during the switch over or delay stages.

RESULTS AND DISCUSSION

Mechanism of the Penetration Behaviors of the Inner Melt and Water at the Curved Sections

Figure 4 shows the interfaces of the skin and inner melts of the test case. As can be seen, both the simulation result and the experimental result show that the residual thicknesses of the skin layer and the inner layer were uniform at the straight segments and nonuniform around the curved sections. A comparison of the experimental and simulation results of the residual thickness of the skin layer and the inner layer at the 11 specified

Table V. Factors and Their Levels in Orthogonal Simulations

Factors	Level 1	Level 2	Level 3
A: Mold temperature (°C)	300	330	360
B: Inner melt temperature (°C)	480	500	520
C: Inner delay time (s)	3	5	7
D: Inner injection velocity (m/s)	0.5	1.0	1.5
E: Water temperature (°C)	300	320	340
F: Water injection delay time (s)	5	10	15
G: Water injection velocity (m/s)	0.5	1.0	1.5

positions are shown in Figure 5. Figure 5 illustrates that both the residual thicknesses of the skin layer and inner layer at the inner concave side (positions 2/3/4 of right side and positions 6/7/8/10/11 of left side) first decreased then increased, while those at the outer convex side (positions 2/3/4 for left side and positions 6/7/8/10/11 for right side) first increased then decreased. This means that the penetrations of the inner melt and water were always close to the inner concave side. This was due to two differences between the inner concave side and the outer convex side: the pressure gradient and the temperature. Figure 6 shows the simulation results at 1.18 s, which was the time that the inner melt began to penetrate through the curved section, as shown in Figure 6(a). Figure 6(b) shows the pressure contours at this moment. As can be seen, the pressure contours near the inner concave side were closer than those near the outer convex side, which means that the pressure gradients near the inner concave side were higher than those close to the outer convex side. Consequently, the velocity near the inner concave side was faster than that close to the outer convex side, as shown in Figure 6(c). Thus, the tip of the inner-melt was biased toward the inner concave side. Meanwhile, the higher shear near the inner concave side led to higher temperatures due to higher shear heating and greater heat concentration. Figure 6(d) shows that the temperature contours near the inner concave side were closer than those near the outer convex side, which means that the cooling was more efficient near the outer convex side for its larger cooling area. Thus, the high-viscosity melt layer near the outer convex side was thicker than that near the inner concave side. These two factors led to the thicker skin layer near the outer convex side as opposed to near the inner concave side. The same thing happened to the water penetration. As we can see from Figure 7, the temperature field near the front of the water was very different from that near the front of the inner melt, which is shown in Figure 6(d), for the cooling of water. There was some low-temperature and high-viscosity melt at the front of the water. It was pushed by the

Table IV. Processing Parameters Used in the Simulations of Variable Geometries

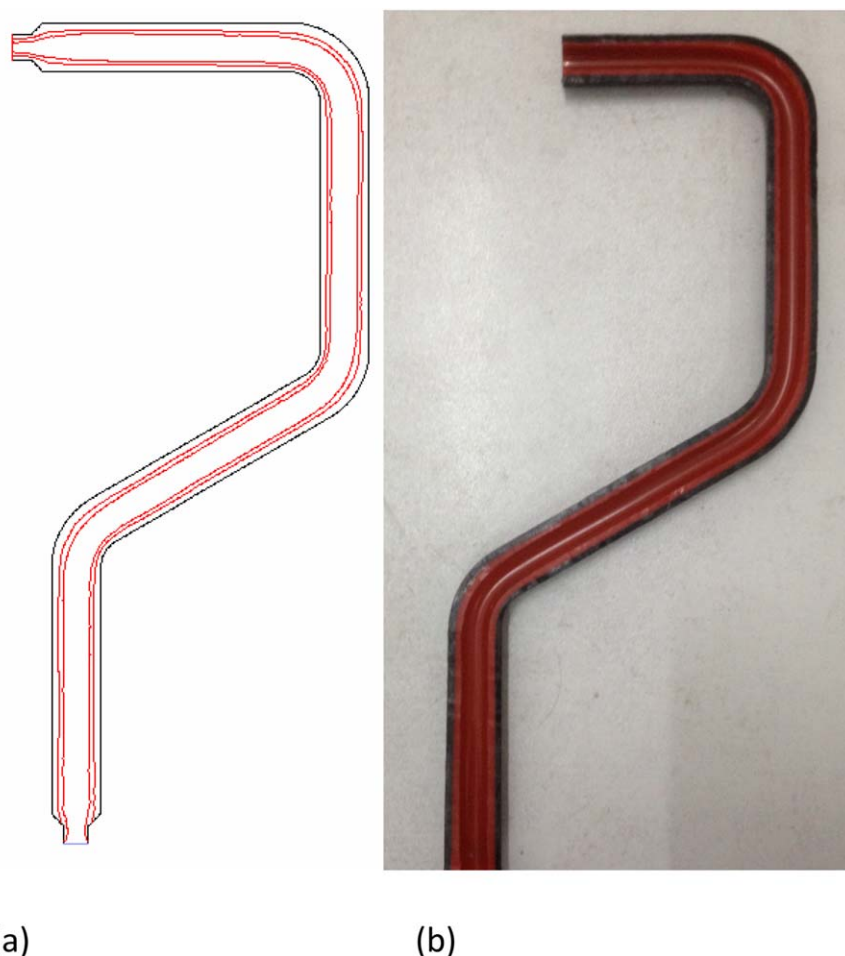| Mold temp. (K)	Skin melt temp. (K)	Inner melt delay time(s)	Inner melt temp. (K)	Inner melt injection velocity (m/s)	Water delay time (s)	Water temp. (K)	Water injection velocity (m/s)
300	520	3	500	1	15	300	1

Figure 4. Interfaces of the skin- and inner melts of the test case: (a) simulation result and (b) experimental sample. [Color figure can be viewed in the online issue, which is available at wileyonlinelibrary.com.]

water along the narrow channel with high temperature and less resistance.

It should be noted that although the numerical results were in good agreement with the experimental results qualitatively, as shown in Figures 4 and 5, the numerical result of the skin layer was overestimated. This may have been due to the constant mold temperature setting in the simulation, while the cavity wall temperature actually increased during the filling stage, especially for the overflow process. The simulation results of the inner layer agreed well with the experimental results quantitatively. This may have been because the mold temperature had little effect on the penetration of the inner melt due to the low thermal conductivity of the skin layer.

Effects of the Bending Radius and the Bending Angle on the Residual Thickness of the Skin and Inner Layers

Figure 8 presents the effect of the bending radius on the penetration interfaces of the inner melt and water based on the simulation. The residual thicknesses of the skin layer at the inner concave side, the inner layer at the inner concave side, the inner layer at the outer convex side, and the skin layer at the outer convex side were calculated and plotted.

The residual thicknesses at the outer convex side were more uniform than those at the inner concave side. This was due to the fact that the transition length from a straight segment to the next straight segment at the outer convex side was longer than that at the inner concave side. Increasing the bending radius increased the uniformity of the residual thicknesses at the inner concave side, especially for the cases where the bending radius was less than three times of the radius of pipe. This was due to the increased bending radius, which caused an increase in the transition length between the two straight segments.

Figure 8 shows that the bending radius has little effect on the residual thicknesses of the skin and inner layers at the outer convex side. This was due to the fact that more effective heat transfer existed at the outer convex side. The increasing bending radius had little effect on further improving the heat transfer efficiency at the outer convex side. Figure 8 shows that the residual thicknesses of the skin layer and the inner layer at the inner concave side increased with increasing bending radius. This may have been due to two facts: (1) increasing the bending radius efficiently improved the heat transfer efficiency at the
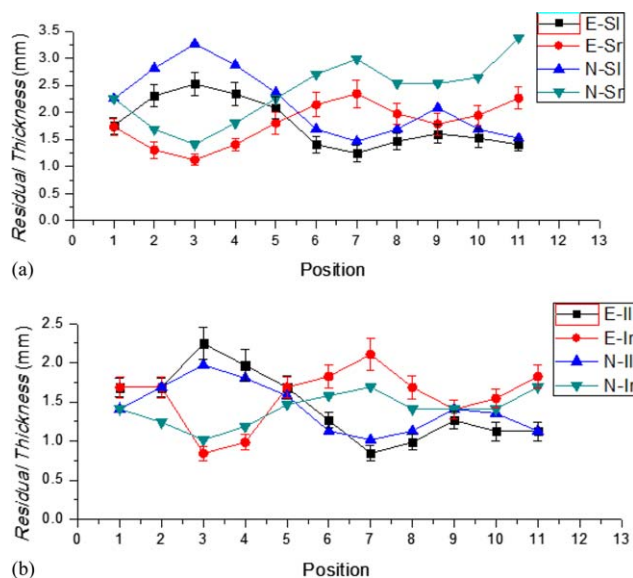
(a)

(b)

Figure 5. Comparison of the experimental and simulation results of the residual thickness of (a) the skin layer and (b) the inner layer. *E* denotes the experimental result. *N* denotes the numerical simulation result. *S* is the skin layer and *I* is the inner layer. *L* is the left side and *r* is the right side. Positions 1, 5, and 9 locate at the middle of straight sections. [Color figure can be viewed in the online issue, which is available at wileyonlinelibrary.com.]

inner concave side and (2) increasing the bending radius decreased the pressure gradient at the inner concave side and thus decreased the velocity and the shear rate near the inner concave side leading to less heat generation and a lower temperature at the inner concave side. Consequently, less melt could be pushed and displaced.

Figure 9 presents the effect of the bending angle on the penetration interfaces of the inner melt and water. The residual thicknesses of the skin and inner layers were calculated and plotted. It is illuminated that both layers at the outer convex side were thicker than those at the inner concave side. Although the residual thicknesses of the skin and inner layers at the inner concave side of the curved section were thinner than those at the straight pipe, the bending angle had little effect on the residual thicknesses of the skin and inner layers at the inner concave side. This may have been because increasing the bending angle had little effect on further worsening the heat transfer efficiency or push material that is already too cold to be displaced at the inner concave side. The residual thickness of the skin layer at the outer convex side increased with increasing the bending angle, which can efficiently improve the heat transfer efficiency at the outer convex side. Furthermore, due to the low thermal conductivity of the skin layer, increasing the bending angle only slightly increased the residual thickness of the inner layer at the outer convex side.

Effects of Processing Parameters on the Residual Thickness of Melts

The residual thicknesses of the skin and inner layers at the inner concave and outer convex sides were recorded and the average residual thicknesses corresponding to the factor levels in the

orthogonal array were calculated. The variation of the residual thicknesses of layers as a function of the factor levels is shown in Figure 10.
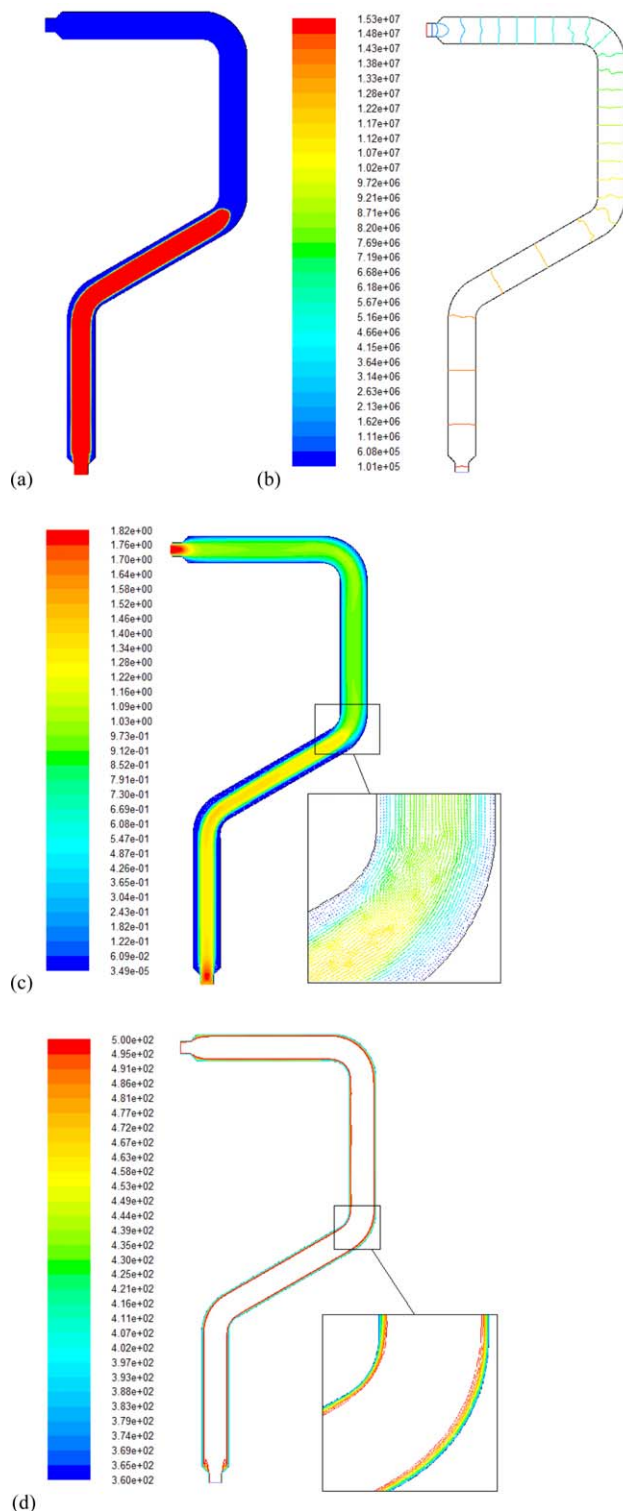

(a)   (b)

(c)

(d)

Figure 6. Simulation results of the test case at 1.18 s: (a) Front position of the inner melt. (b) Pressure contours. (c) Velocity field. (d) Temperature field. [Color figure can be viewed in the online issue, which is available at wileyonlinelibrary.com.]
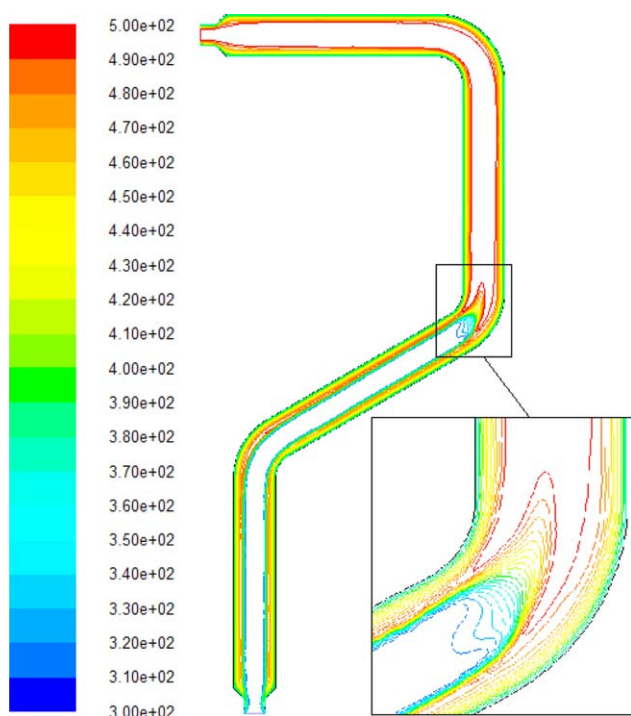
Figure 7. Temperature field at 1.18 s of the test case. [Color figure can be viewed in the online issue, which is available at wileyonlinelibrary.com.]
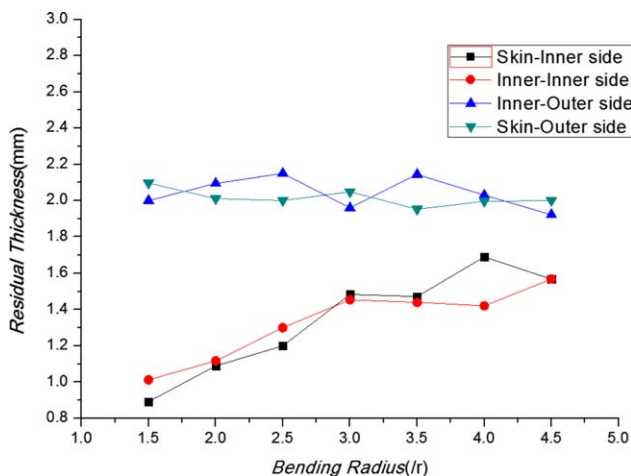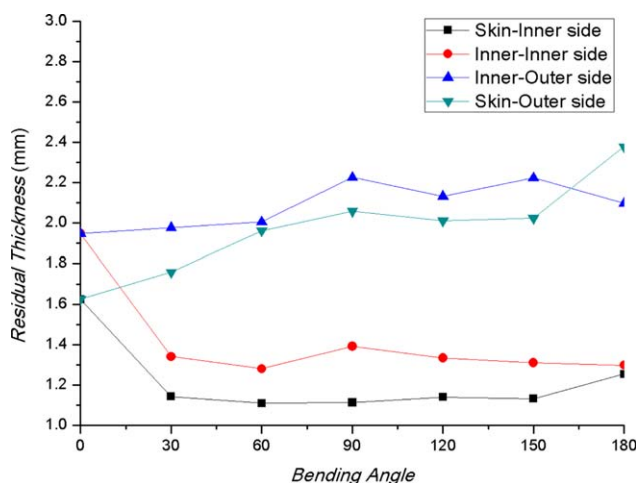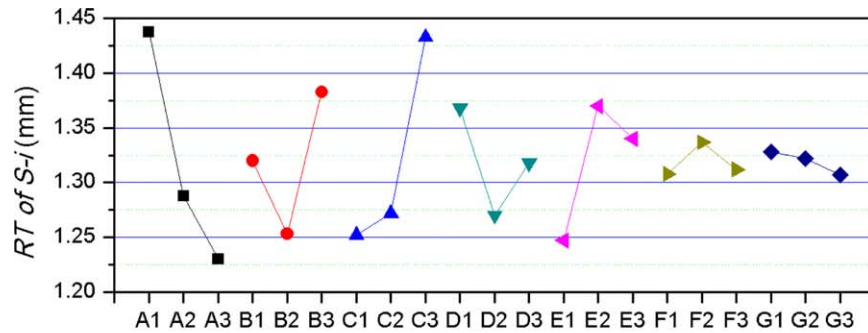

Figure 9. Residual thicknesses of cases with different bending radiuses. [Color figure can be viewed in the online issue, which is available at wileyonlinelibrary.com.]

As can be seen from Figure 10, the main factors affecting the skin layers at the inner concave side and the outer convex side were the mold temperature and the inner melt injection (switch over) delay time. The skin layer at the inner concave side became thicker with decreasing mold temperature and increasing inner melt injection delay time, as shown in Figure 10(a,d). This was due to the lower mold temperature and the longer inner injection delay time increasing the thickness of the solidified layer of the skin melt and correspondingly decreasing the cross-section of the inner melt penetration.

For the inner layer at the inner concave side, the residual thickness was mainly influenced by the factors of the inner melt

Figure 8. Residual thickness for cases with different bending radiuses. [Color figure can be viewed in the online issue, which is available at wileyonlinelibrary.com.]

injection delay time and the inner melt temperature, as shown in Figure 10(b), due to the fact that the longer inner melt delay time led to an increase in the solidified layer thickness of the skin melt especially on the outer convex side, further pushing the penetration of water closer to the inner concave side. Consequently, the residual thickness of the inner layer at the inner concave side decreased with increasing inner melt injection delay time. The inner layer at the inner concave side increased with increasing inner melt temperature. This can be explained by the higher inner melt temperature leading to lower viscosity and less resistance to water penetration. Also, the difference in pressure gradient between the inner concave side and the outer convex side became less. Correspondingly, the penetration of water was closest to the middle of the curved section.
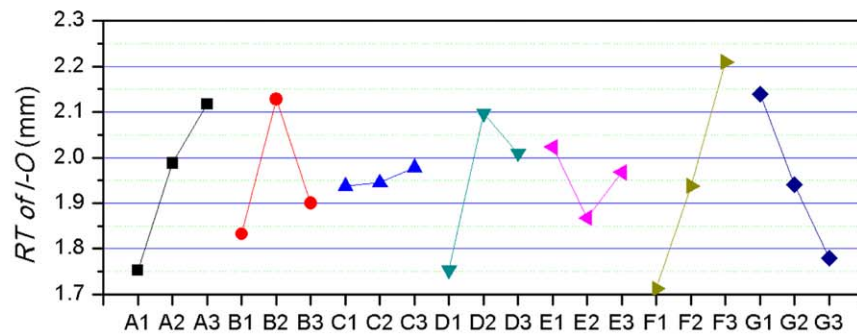
For the inner layer at the outer convex side, the main influence factors for residual thickness were the water injection delay time, mold temperature, and water injection velocity. From Figure 10(c), it can be seen that the residual thickness of the inner layer at the outer convex side increased with increasing mold temperature. This was due to the mold temperature having a much greater effect on the temperature field near the outer convex side than near the inner concave side. The higher mold temperature decreased the thickness of the outer solidified layer of the skin melt and decreased the viscosity of the melt near the outer convex side. Consequently, the penetration of inner melt was closest to the outer convex side, while the penetration of water was closest to the inner concave side. The residual thickness of the inner layer at the outer convex side increased with increasing water injection delay time, as shown in Figure 10(c). This was because the longer water injection delay time increased the viscosity of the melt near the outer convex side, while it has less effect on the melt near the inner concave side. The penetration of water was closer to the inner concave side. It can be seen from Figure 10(c) that the inner layer at the outer convex side became thinner with increasing water injection velocity. This can be explained by the higher water injection velocity causing more of the inner melt near the outer convex side to be
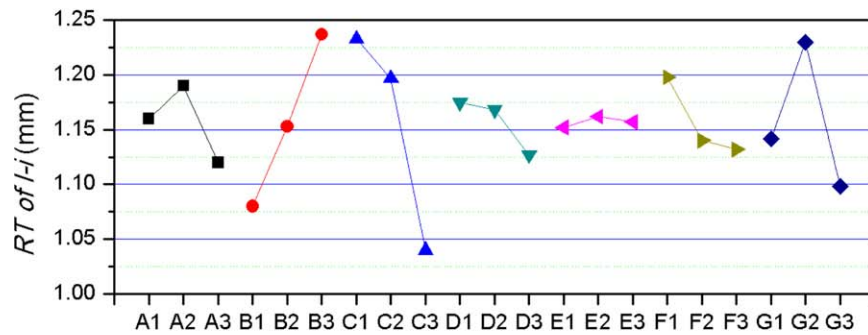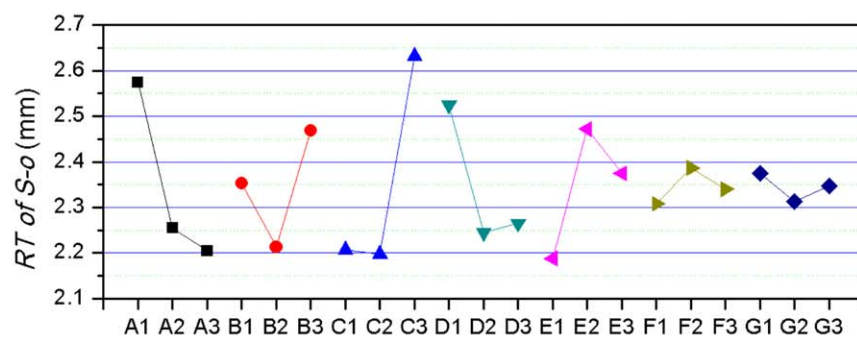
Figure 10. Variation of the residual thicknesses of (a) the skin layer at the inner concave side, (b) the inner layer at the inner concave side, (c) the inner layer at the outer convex side, and (d) the skin layer at the outer convex side with factor levels. [Color figure can be viewed in the online issue, which is available at wileyonlinelibrary.com.]

displaced by the water for the water inertia being taken into account in these simulations.

CONCLUSIONS

A CFD numerical program has been developed to simulate the O-WACIM process. The simulation results in terms of the skin layer were in good agreement with the experimental data. The penetrations of the inner melt and water were always closest to the inner concave side due to the higher local pressure gradient and temperature.

The bending radius was found to have little effect on the residual thicknesses of the skin and inner layers at the outer convex side. Increasing the bending radius increased the residual thicknesses of the skin layer and the inner layer and those uniformity at the inner concave side.

The bending angle had little effect on the residual thicknesses of the skin and inner layers at the inner concave side. The residual thickness of the skin layer at the outer convex side increased with increasing bending angle.

The main factors that affected the skin layers were the mold temperature and the inner melt injection delay time. The skin layer at the inner concave side became thicker with decreasing mold temperature and increasing inner melt injection delay time.

The residual thickness of the inner layer at the inner concave side increased with decreasing inner melt injection delay time and increasing inner melt temperature. The residual thickness of the inner layer at the outer convex side increased with increasing water injection delay time and mold temperature and decreasing water injection velocity.

REFERENCES

1. Lang, S.; Parkinson, M. J. *J. Plast. Rubber Compos.* **2005**, *34*, 232.

2. Linse, F.; Giessauf, J.; Steinbichler, G. *Kunststoffe International* **2007**, *11*, 68.

3. Knights, M. *Plast. Tech.* **2002**, *48*, 42.

4. Liu, S.-J.; Chen, Y.-S. *Polym. Eng. Sci.* **2003**, *43*, 1806.

5. Park, H. P.; Cha, B. S.; Park, S. B.; Choi, J. H.; Kim, D. H.; Rhee, B. O.; Lee, K. H. *Adv. Mat. Sci. Eng.* **2014**, DOI: 10.1155/2014/238251.

6. Seldén, R. *Polym. Eng. Sci.* **2000**, *40*, 1165.

7. Kim, N. H.; Isayev, A. I. *Polym. Eng. Sci.* **2014**, DOI: 10.1002/pen.23871.

8. Liu, S. J.; Wu, Y. C.; *Polym. Test.* **2007**, *26*, 232.

9. Polynkin, A.; Bai, L.; Pittman, J. F. T.; Sienz, J.; Mulvaney-Johnson, L.; Brown, E.; Dawson, A.; Coates, P.; Brookshaw, B.; Vinning, K.; Butler. *J. Plast. Rubber Compos.* **2008**, *37*, 131.

10. Ahmad, Z. A.; Amir, H. B. *Polim. W.* **2009**, *54*, 564.

11. Kuang, T. Q.; Yu, C. C.; Deng, Y.; Zhang, K. *J. Chem. Ind. Eng.* **2014**, *65*, 4176.

12. Chen, Y. L.; Zhou, H.; Zhang, Z. M.; Kong, H. Z. *China Plast.* **2012**, *26*(6), 72.

13. Huang, H. X.; Deng, Z. W. *J. Appl. Polym. Sci.* **2008**, *108*, 228.

14. Yang, J. G.; Zhou, X. H.; Luo, G. P. *Int. Adv. Manu. Tech.* **2013**, *69*, 2605.

15. Jian Gen, Yang; Xiong Hui, Zhou; Qiang, Niu *Int. Adv. Manuf. Tech.* **2013**, *67*, 367.

16. Kuang, T. Q.; Deng, Y. *China Plast.* **2014**, *28*(2), 96.

17. Zhang, S.; Cao, W.; Zheng, G.; Jia, Z.; Shen, C. *Int. Poly. Proc.* **2011**, *26*, 560.

18. Khor, C. Y.; Ariff, Z. M.; Ani, F. C.; Mujeebu, M. A.; Abdullah, M. K.; Abdullah, M. Z.; Joseph, M. A. *Int. Commun. Heat Mass* **2010**, *37*, 131.

19. Zhang, K.; Kuang, T. Q.; Liu, H. S.; Zeng, X. S.; Deng, Y.; Hrvoje Jasak. *Polym. Mat. Sci. Eng.* **2014**, *30*(9), 93.

20. Kuang, T. Q.; Deng, Y. *China Plast.* **2013**, *27*(1), 106.

21. Zhang, K.; Kuang, T. Q.; Liu, H. S.; Zeng, X. S. *Polym. Mat. Sci. Eng.* **2013**, *29*(11), 178.

22. Zhou, G. F.; Chao, F. C.; Zhang, Y. *Eng. Plast. Appl.* **2013**, *41*(1), 47.

23. Kuang, T. Q.; Deng, Y.; Yu, C. C.; Zhou, K.; Turng, L. S. ANTEC Conference Proceedings; Orlando: USA, **2015**.

24. Liu, S. J.; Lin, C. H. *J. Reinf. Plast. Comp.* **2007**, *26*, 1441.

25. Lin, K. Y.; Chang, F. A.; Liu, S. J. *Int. Commun. Heat Mass* **2009**, *36*, 491.

26. Yang, J. G.; Zhou, X. H. *J. Appl. Polym. Sci.* **2013**, *128*, 1987.

27. Hieber, C. A.; SHEN, S. F. *J. Non-Newtonian Fluid Mechanics* **1980**, *7*, 1.

28. Zhou, H. Computer modeling for injection molding: simulation, optimization, and control; John Wiley & Sons: Hoboken, New Jersey, **2013**.

29. Frisch, U. Turbulence: the legacy of A. N. Kolmogorov; Cambridge University Press: Cambridge, **1995**.

30. Zhao, P.; Zhou, H. M.; Li, Y.; Li, D. Q. *Int. Adv. Manu. Tech.* **2010**, *49*, 949.